MULTISCALE MODEL. SIMUL.
Vol. 1, No. 1, pp. 25–39

TOWARDS MULTISCALE MODELING OF METALS VIA EMBEDDED PARTICLE COMPUTER SIMULATION*

MARTIN KRÖGER†, IGOR STANKOVIC‡, AND SIEGFRIED HESS‡

Abstract. The embedded atom method is adapted to study solid friction and the mechanical behavior of a model metal which incorporates the effect of electronic glue in its structure. The elastic properties of real metals are reproduced by a set of basic model potentials as revealed by analytic considerations. A slightly modified version of a classical nonequilibrium molecular dynamics computer simulation is employed to study the dynamics and structural changes of the model metal undergoing a process of solid friction and an uniaxial compression in order to analyze, e.g., plastic yield, transient friction coefficients, and the underlying structure. Under the appropriate choice of parameters, the model turns out to also be applicable for studying multiscale structures in porous metals.

Key words. embedded particle, molecular dynamics, metal, solid friction, elasticity, plasticity, foam, sponge

AMS subject classifications. 74F, 74C20, 82D35

PII. S1540345902408470

1. Introduction.

In the early 1980s the theoretical investigation of hydrogen embrittlement gave rise to a systematic modeling and simulation approach towards generic models for metals. A fundamental understanding of the atomistic processes involved in hydrogen embrittlement had been impossible, largely because of difficulties in the theory of such complicated systems. Traditional monoscale approaches such as ab initio techniques had proven to be inadequate, even with the largest supercomputers, because of the range of scales and the prohibitively large number of atoms involved. The embedded atoms method overcomes the fundamental limitation of past methods such as pair potentials and yet is practical enough for the calculation of defects, surfaces, and impurities in metals on multiple scales. Ab initio methods are still incapable of handling the large numbers of atoms required to represent fracture. Even the capacity of one-electron methods [1] falls far short of the number of atoms required to simulate fracture. The use of pairwise interaction greatly increases the number of atoms that can be treated [2, 3] but requires a volume-dependent term to represent the bulk compressibility of the electron gas [4, 5]. Volume dependence restricts the use of pair potentials to situations where the volume is definable; it is not restricted during fracture.

The quasi-atom theory [6, 7] (or effective medium) had been used successfully to calculate the characteristics of hydrogen in metals. In [8, 9] the theory was generalized to treat all atoms in a unified way [10, 11]. The method is called "embedded particle method" because it views each particle as embedded in a host lattice consisting of all

*Received by the editors May 25, 2002; accepted for publication (in revised form) August 26, 2002; published electronically January 28, 2003. This work was supported by the Deutsche Forschungsgemeinschaft (DFG) via the special research area Sfb 448 "Mesoskopisch strukturierte Verbundsysteme."

http://www.siam.org/journals/mms/1-1/40847.html

†Institut für Theoretische Physik, Fakultät II, Technische Universität Berlin, D-10623 Berlin, Germany. Current address: Polymer Physics, Material Sciences, ETH Zürich, CH-8092 Zürich, Switzerland (kroeger@ar.ethz.ch).

‡Institut für Theoretische Physik, Fakultät II, Technische Universität Berlin, D-10623 Berlin, Germany (stankovic@itp.physik.tu-berlin.de, s.hess@physik.tu-berlin.de).

other particles. Such a view permits calculations employing an electron density, which is always definable, and allows realistic treatment of impurities in structures that include cracks, surfaces, impurities, and alloying additions [8, 9, 11]. The generalized method is not significantly more complicated to use than pair potentials. It had been used in a number of recent works; see, e.g., [12, 13, 14, 15, 16, 17, 18]. Solution of the Schrödinger equation yields the electron density established by a given potential, and the energy is a functional of that potential. Hohenberg and Kohn [19] show the converse: the energy is a functional of the density, and the potential is determined to within an additive constant by its electron density. Scott and Zaremba [6] proved that the energy of an impurity in a host is a functional $\mathcal{F}$ of the electron density of the unperturbed (i.e., without impurity) host. This statement is that the embedding density of an impurity is determined by the electron density of the host before the impurity is added. The embedded atoms method makes use of this by viewing each atom in a system as an impurity in the host consisting of all other atoms.

The functional $\mathcal{F}$ is universal, independent of the host. Its form, however, is unknown. A simple approximation would be to assume that the embedding energy depends only on the environment immediately around the impurity [7], or, equivalently, that the impurity experiences a locally uniform electron density [6]. This can be viewed as either a local approximation or as the lowest-order term involving successive gradients of the density. Then the functional is approximated by a function of the electron density at the impurity site plus an electrostatic interaction Φ, and the total energy is written as a sum over all individual contributions. Because the functions $\mathcal{F}$ and Φ are not known in general, in [8, 9] experimental data had been used to determine functions. Both functions are required to fit the elastic properties such as the Cauchy discrepancy. In the early works [8, 9], $\mathcal{F}$ was taken from electron gas computations provided in [20].

In this work we introduce a set of particularly simple and generic model potentials motivated through semiempirical calculations which are expected to describe the mechanical properties of metals ranging from the nanometer scale (asperites) up to the macroscopic scale (solid friction, metal foams). Our model is characterized by a few model parameters such as reference energy, time, and length. Properties of the model are obtained in terms of these reference values. Constitutive relationships between stress and deformation obtained from our model serve to enter conventional solvers when complex geometries are considered. It will be shown that elastic properties of real metals are reproduced by the set of basic model potentials as revealed by analytic considerations. The goal will be to analyze preliminary results of the novel model and the range of its application in a qualitative fashion.

In this work we further demonstrate that—and show how—the proposed model for a bulk metal can be used to study metal sponges and porous metal structures. Metal sponges and foams show some potential for being produced with controlled spatial variations in their density. This suggests employing them as graded materials in space filling lightweight structures in analogy to cortical bone, a natural cellular material, that displays increased density in regions of high loading. Most mechanical and physical properties are affected by the porosity as well as the size of the pores and at the same time by the thickness of the structured studs of the metal sponge. The past few years have seen increasing interest in porous metallic materials, especially in foams made of aluminum or aluminum alloys. The stimulus for this lies in recent process developments which promise materials with better quality and lower costs. Moreover, the environment for the application of new materials of this type

has greatly changed. Now higher demands for passenger safety in automobiles or for easy materials recycling make metal foams and sponges attractive where, a few years ago, the same materials would have been ruled out for technical or economical reasons [21]. The mechanical performance of metal foams governs their utility in various applications, such as cores for ultralight sandwich panels/shells, as well as crash or blast absorbing systems. Macroscopic stress/strain characteristics establish their performance. Most important are the stiffness, the yield strength, and the "plateau" stress at which the material compresses. Once these have been measured, continuum mean-field constitutive relations can be implemented [22] for the study of structural competitiveness; cf. [23] and references cited therein. Such homogenized treatments are applicable to structures that encompass many cells. For structures embracing few cells, recognition must be given to a material length scale that depends on the microscopic mechanisms of deformation at the cell level. In order to clarify notation, due to the generic choice of model potentials in the following, the spatial coordinate of a "particle" may represent either the position of a "model nucleus" or the position of a spatially localized number of nuclei. Positions of the electrons are not considered explicitly; their motion will be effectively captured through the embedding density and the embedding functional.

2. The framework. In order to study the mechanical properties of a model metal, including solid friction, uniaxial compression, shear deformation of bulk metals, and porous metal structures, we adapt the embedded atom method in the spirit of Holian et al. [24]. The method, originated by Daw and Baskes [8, 9], resembles the fact that in metals the conduction electrons are not localized about the nuclei; the energy depends upon the local electron density, resulting in forces between particles that are many body in character, rather than simply pairwise additive [25]. Accordingly, one considers two contributions to the potential energy E of the whole system made up of N particles. There is a conventional binary interaction term through a two-body interaction potential Φ as a function of the distance between interaction sites and a term stemming from an embedding functional $\mathcal{F}$, which produces the effect of the electronic "glue" between interaction sites:

$$E_{\mathrm{b}} = N\, e_{\mathrm{b}} = \sum_{i=1}^{N} \left(\frac{1}{2} \sum_{j \neq i}^{N} \mathrm{e}_{ij} \Phi(\mathbf{r}^{ij}) + \mathcal{F}(\rho_i) \right), \tag{2.1}$$

where $e_{\mathrm{b}} = E_{\mathrm{b}}/N$ represents a "binding energy" per particle. The quantity $\mathcal{F}$ is a nonlinear function of the (local) embedding density ρ_i of atoms $i = 1, \ldots, N$. It is constructed from the radial coordinates of surrounding particles and requires the choice of a weighting function $w(r)$:

$$\rho_i = \sum_{j} \mathrm{w}_{ij} w(\mathbf{r}^{ij}) = w(0) + \sum_{j \neq i} \mathrm{w}_{ij} w(\mathbf{r}^{ij}), \tag{2.2}$$

where $\mathbf{r}^{ij} \equiv \mathbf{r}^i - \mathbf{r}^j$ is the relative position vector between particle coordinates $\mathbf{r}^i$ and $\mathbf{r}^j$. For the study of bulk metals the coefficients e_{ij} and w_{ij} are irrelevant and set to unity. For the case of solid friction, where two metals are in contact, they become relevant and model the properties of the interface (contact zone). They allow us to specify the strength of interaction between particles belonging to the same and to different materials; i.e., we have $\mathrm{w}_{ij} = \mathrm{w}_{aa} = \mathrm{w}_{bb}$ =fixed for particles i, j of the same metal, and $\mathrm{w}_{ij} = \mathrm{w}_{ab}$ =fixed for a pair of "different" specimen i, j. The same

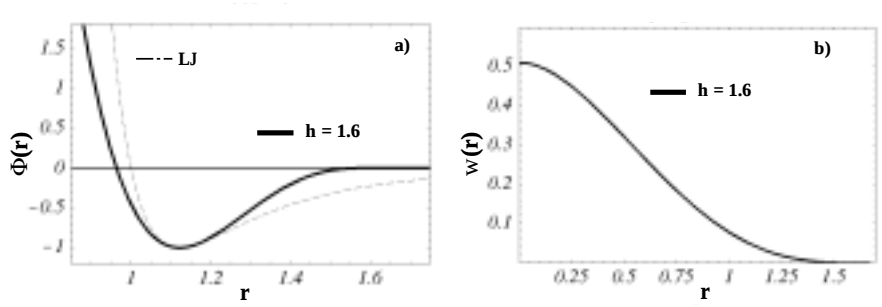

FIG. 1. *Left: The binary interaction potential used in the nonequilibrium molecular dynamics (NEMD) simulations is plotted together with a Lennard–Jones (LJ) potential, both in dimensionless LJ units; i.e., r stands for r/r_0. The potential cutoff h is a model parameter. Right: The (normalized) Lucy weight function $w(r)$ vs. distance r in LJ units is used to calculate embedding densities for all atoms. These densities enter the embedding ("glue") functional $\mathcal{F}$.*

potentially applies to e_{ij}. If not explicitly specified, we have $\mathrm{w}_{ij} = \mathrm{e}_{ij} = 1$ in the following.

Parts of $\mathcal{F}$ linear in ρ_i can be combined with the original repulsive two-particle potential to an effective potential Φ used here which also has an attractive part. Corrections can be included in (2.1) for involving gradients of the density [6]; these do not modify the form of (2.1). It is implicitly assumed that the electron density is given by a linear superposition of the electron densities of the constituent atoms [26]. Ground-state properties of the solid can be calculated from (2.1) in a straightforward way (e.g., by using the conjugate gradients technique).

3. Particular choice of model potentials. A simple choice for the model functions Φ, w, and $\mathcal{F}$ leads to our generic model metal, denoted as EMB in the following. For the binary potential function Φ we use a radially symmetric short ranged attractive (SHRAT) potential $\Phi(r)$,

$$\Phi(r) = \phi_0\, r_0^{-4} \left[3(h-r)^4 - 4(h-r_{\min})(h-r)^3\right], \tag{3.1}$$

for $r \le h$ and $\Phi(r) = 0$ otherwise, with an energy scale ϕ_0, a length scale r_0, and an interaction range h. The minimum of the potential (see Figure 1) is located at the distance $r = r_{\min} = 2^{1/6}\, r_0 \approx 1.123\, r_0$ as for a LJ potential, and the well depth of the potential is $-\Phi(r_{\min}) = \phi_0\, r_0^{-4}(h - r_{\min})^4$. Properties of the (pure) SHRAT model system in its gaseous, (metastable) liquid, and solid states have been computed recently by molecular dynamics and compared with analytical calculations in [27]. The elastic behavior of the SHRAT model has been characterized by the bulk and shear moduli, and their corresponding Born–Green and fluctuation contributions. Stick-slip behavior, and the detailed elastic response and plastic flow of the model solid has been analyzed, and the transition from the elastic to the plastic behavior has been approximately described by a generalized Maxwell–Kelvin–Voigt model for the stress tensor [27].

For reasons discussed in [24, 28] we use the normalized Lucy's weight function (see Figure 1) in the definition (2.2) of the embedding density; i.e.,

$$w(r) = w_0 \left(1 + 3\,\frac{r}{h}\right)\left(1 - \frac{r}{h}\right)^3 \tag{3.2}$$

TABLE 1

Reference values for a set of metals, including the model metal EMB (all parameters $n, \rho_{\rm des}, F_0$ are equal to unity), together with reported values for the elastic modulus E, the shear modulus G, and the elastic anisotropy $c_{\rm ani} \equiv 2c_{44}/(c_{11}-c_{12})$; the coefficients c_{ij} denote Voigt moduli [36].

Metal	$n_{\rm ref}$	$T_{\rm ref}$	$P_{\rm ref}$	E	G	$c_{\rm ani}$
Ag	59.4 $\rm nm^{-3}$	34.3 kK	28 GPa	101 GPa	38 GPa	2.99
Cu	85.5 $\rm nm^{-3}$	40.6 kK	48 GPa	156 GPa	59 GPa	3.19
EMB	72.5 $\rm nm^{-3}$	40.0 kK	40 GPa	260 GPa	95 GPa	2.56
Fe	85.2 $\rm nm^{-3}$	49.8 kK	59 GPa	232 GPa	94 GPa	2.32
Ni	92.0 $\rm nm^{-3}$	51.8 kK	65 GPa	239 GPa	101 GPa	2.39

for $r \le h$ with a prefactor obtained by normalizing the weight function, $w_0 = w(0) = 105/(16\pi h^3)$. The particular simple parabolic embedding potential for EMB is

$$\mathcal{F}(\rho) = F_0\,\phi_0\,r_0^6\,\left((\rho-\rho_{\rm des})^2 - (w_0-\rho_{\rm des})^2\right) + \dots\,, \tag{3.3}$$

where $\rho_{\rm des}$ is the desired embedding number density and F_0 is the embedding strength; the dots denote higher-order terms in $(\rho-\rho_{\rm des})$ which may be considered in order to obtain more than a qualitative agreement between theory and experiments with respect to the quantities listed in Table 1. Other forms for the embedding functional had been used; cf. [11]. Throughout this work we investigate the "basic" model metal for which particle number density $n \equiv N/V = r_0^{-3}$, interaction range $h = 1.6\,r_0$, and the temperature $k_BT = 0.01\phi_0$ are fixed. For the study of bulk metals the desired embedding density equals the particle number density, i.e., $\rho_{\rm des} = n$; for the case of a metal sponge we choose $\rho_{\rm des} > n$.

4. Scaled quantities and elastic properties of EMB. To compare with experimental data one has to estimate reference values for dimensionless simulation quantities $Q_{\rm dimless}$. For any measurable quantity Q with a dimension specified in SI units kg, m, and s one has $Q = Q_{\rm dimless}Q_{\rm ref}$ and

$$Q_{\rm ref} = m^{\alpha+\gamma/2} r_0^{\beta+\gamma} \phi_0^{-\gamma/2} \quad \text{for } [Q] = \mathrm{kg}^\alpha \mathrm{m}^\beta \mathrm{s}^\gamma, \tag{4.1}$$

where m, r_0, and ϕ_0 provide the scales via the binary interaction potential (3.1) and the equations of motion. The reference values for length r, number density n, energy k_BT (and binding energy per particle $e_{\rm b}$), pressure P, and the elastic moduli in terms of the simulation parameters are therefore $r_{\rm ref} = r_0$, $n_{\rm ref} = r_0^{-3}$, $e_{\rm b,ref} = \phi_0 = k_{\rm B}T_{\rm ref}$, and $P_{\rm ref} = \phi_0 r_0^{-3} = n_{\rm ref} e_{\rm b,ref}$. On the other hand, reference values for real masses $m_{\rm ref}$, densities $n_{\rm ref}$, and binding energies $e_{\rm b}$ can be inferred from the literature; see Table 1 for sample values. For Ag, e.g., one obtains model parameters $r_0 = n_{\rm ref}^{-1/3} = 2.56\,\text{Å}$, $\phi_0 = 47.4 \times 10^{-18}\,\rm J$, and $m = 1.790 \times 10^{-21}\,\rm kg$. The values for the moduli of the model metal EMB at $n = 1$ and $F_0 = 1$ are obtained from deformations of a perfect fcc crystal. For plots of the binding energy and pressure for perfect fcc and bcc lattices, see Figure 2. By choosing $T_{\rm ref} = \phi_0/k_{\rm B} \equiv 40\,\rm kK$, $P_{\rm ref} \equiv 40\,\rm GPa$ one arrives at $n_{\rm ref} = 72.5\,\rm nm^{-3}$ and $r_0 = 2.4\,\text{Å}$. For $m = 1.790 \times 10^{-25}\,\rm kg$ the reference time is $t_{\rm ref} = r_0\,(m/e_{\rm b,ref})^{1/2} = 1.3 \times 10^{-13}\,\rm s$ for EMB. The squared reference time for the model system $t_{\rm ref}$ therefore scales linearly with the mass of a particle or an agglomerate of particles, if the agglomerate is considered as reference unit, and may be of the order of seconds concerning the adapted model for porous metal structures to be discussed below. The behavior of a particular material can be described in detail by considering an additional model parameter in (3.3), but this is not done here. The values of the elastic anisotropy and the shear modulus are within the expected ranges for fcc metals; the elastic modulus is slightly higher for EMB.

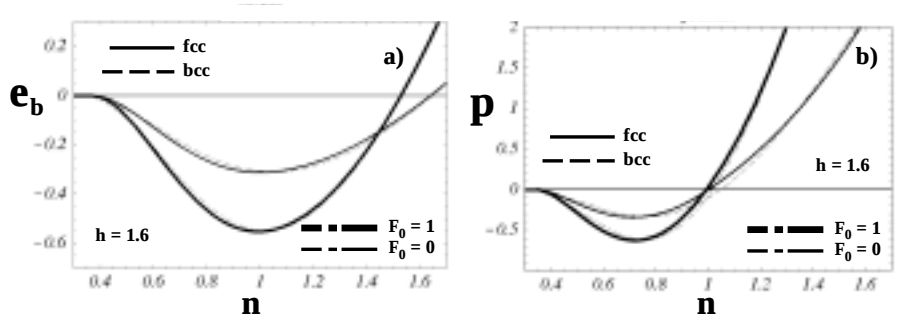

FIG. 2. *The binding energy* e_b *per particle (left) and the hydrostatic pressure (right) vs. density (both in LJ units) at* $h = 1.6$ *for ideal fcc and bcc lattices and two different amplitudes of the embedding functional:* $F_0 = 0$ *and* $F_0 = 1$.

5. Numerical solution. The force acting on particle i is obtained by variation of the energy $\delta E_b = \mathbf{F}_i \delta \mathbf{r}^i$ of (2.1) and yields

$$\mathbf{F}_i = -\sum_{j \neq i} \left(e_{ij} \frac{\partial \Phi}{\partial \mathbf{r}^{ij}} + \left(\frac{\partial \mathcal{F}}{\partial \rho}\Big|_i + \frac{\partial \mathcal{F}}{\partial \rho}\Big|_j \right) \frac{\partial w}{\partial \mathbf{r}^{ij}} \right), \tag{5.1}$$

where $\partial \mathcal{F}/\partial \rho|_i$ is evaluated with embedding density ρ_i. The equations of motions were integrated by a velocity-Verlet algorithm with the force (5.1). The parameters $h, T, \rho_{\mathrm{des}}$ and the average particle density $n = N/V$ are fixed by the model. The influence of the embedding functional $\mathcal{F}$ is estimated by varying its strength F_0. A flow simulation introduces further independent variables, which describe the geometry and strength of flow. For details of a NEMD simulation algorithm, the implementation of Lees–Edwards boundary conditions and periodic images, the homogeneous temperature control under shear and elongational flows, and evaluation of the stress tensor, see, e.g., [29, 30, 31, 32]. The simple model metal EMB is explicitly determined by the set of model potentials and solved without approximations with computational effort of order N.

6. Viscoplastic behavior of EMB. When metal is subjected to stress, it responds by deforming. If only small stresses are applied, then the material returns to its original shape when the stress is relieved. In this regime, metals are elastic; if, however, the stress exceeds a threshold, then the metal suffers permanent plastic deformation. Usually, the kinematics of a three-dimensional continuum, the thermodynamics of materials, and the physics of microscopic defects enter the description of plastic phenomena. A principal feature of plastic behavior is irrecoverable deformation. On a microscopic level, this behavior is caused by defects in the atomic formation of dislocations, dislocation pileup at grain boundaries, polycrystallinity, and anisotropy. A general thermodynamic treatment of phenomenological models has been given, e.g., by Green and Naghdi [33, 34].

Here we report about results obtained by the complementary approach. NEMD computer simulations are performed to study the dynamics and structural changes of the model metal EMB undergoing elongation and shear deformation. The results for the case of shear deformation reveal the influence of initial crystal orientation on transient flow behaviors, the formation of shear bands and dislocations, and the general rate dependence of metal flow behavior in the viscoplastic (strong) flow regime. A profile unbiased temperature control mechanism [35] is used here.

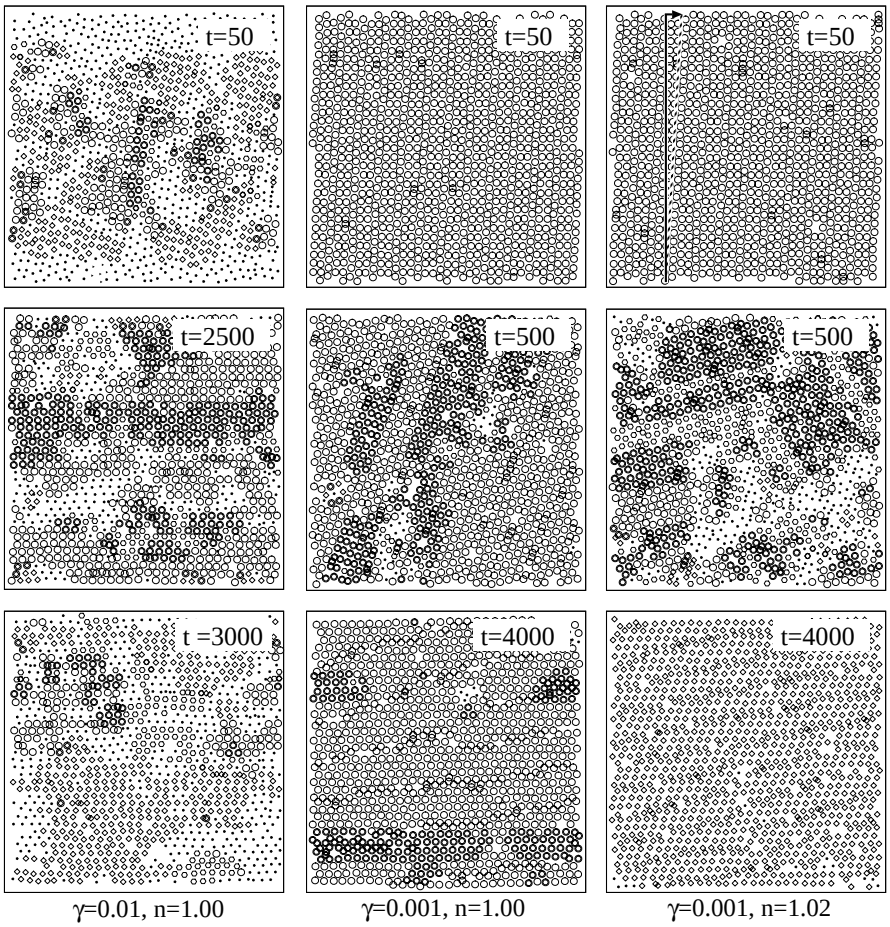

FIG. 3. *Snapshots (including structure analysis) of an EMB metal subjected to simple shear deformation at shear rate $\dot{\gamma}$, particle number density n, and time t (all in reduced units). The snapshots show a cut (width $\triangle r = 1$) of the full system; the direction of shear is depicted in the top right snapshot. Structure recognized by the method presented in* [40] *is encoded as follows: fcc (open spheres), bcc (diamonds), hcp (hexagon within sphere, or bold sphere), and isotropic (filled sphere). Shear induced breakup of structure is observed. For example, at the highest density a polycrystalline conformation with rotating entities is observed (and finally a bcc dominated structure), whereas for smaller densities a more homogeneous evolution (towards fcc) is visible from the plots.*

6.1. Shear flow. Figure 3 shows a time series for a subsystem of a cubic cell with $N = 44000$ particles undergoing shear at two different densities $n = 1$ and $n = 1.02$ and small and intermediate rates $\dot{\gamma} = 0.001$ and $\dot{\gamma} = 0.01$, respectively. The snapshots (including structure analysis) show a cut (width $\triangle r = 1$) of the full system; the direction of shear is depicted in the top right snapshot. Structure is recognized by the method presented in [40]. The top left and centered graphs correspond to an equal amount of deformation $\dot{\gamma}t$; the left column is for a system with shear rate by a factor 10 larger than for the remaining columns. The right column is for a density slightly larger than for the left columns. Shear induced breakup of structure is observed. For example, at the highest density a polycrystalline conformation with rotating entities is observed (and finally a bcc dominated structure), whereas for smaller densities a

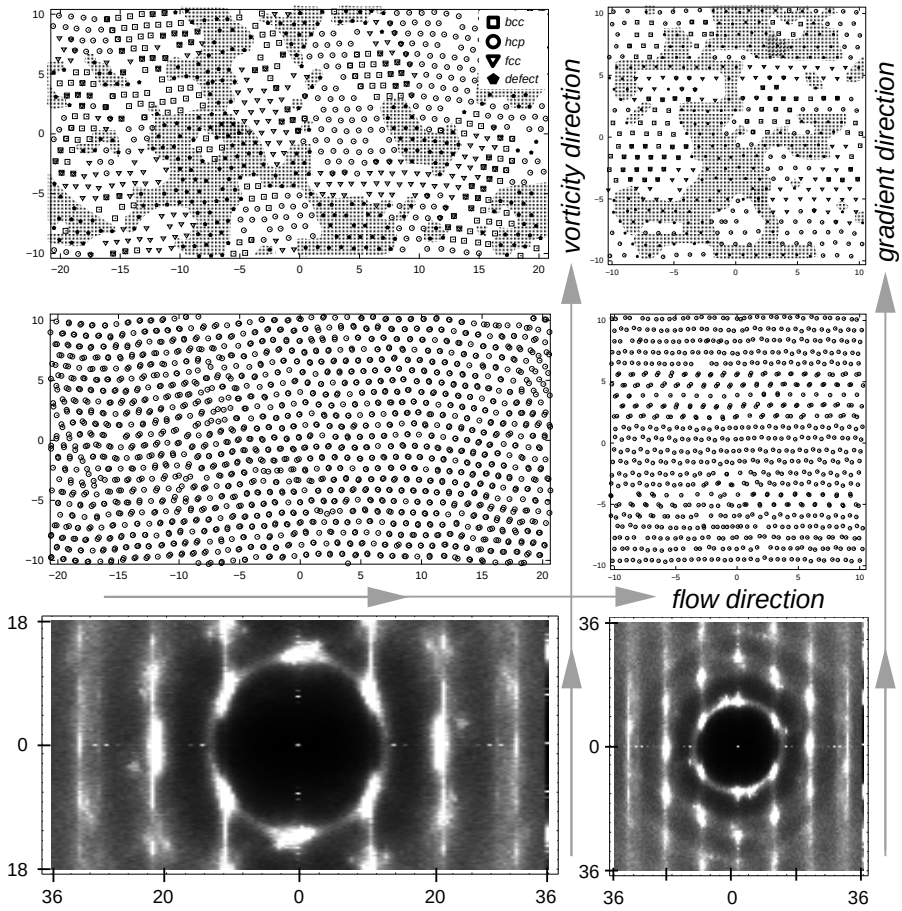

FIG. 4. *NEMD snapshots of the model metal EMB ($N = 16400$ particles, $n = \rho_{\mathrm{des}} = F_0 = 1$) indicating the type of local structure at $t = 2000$ after start of steady shear flow with shear rate $\dot{\gamma} = 0.01$ (flow, gradient, and vorticity direction are specified in the figure). The start configuration is a fcc lattice. Cross-sections of the system are presented, one length unit wide. The method to analyze fcc, bcc, hcp, and icosahedral structure is described (and software is provided) in* [40]. *In the bottom part of the figure the structure factor (see, e.g.,* [30]*) for the same system, projected onto two specified planes, is plotted.*

more homogeneous evolution (towards fcc) is visible from the plots.

A structural analysis and structure factors for a sample snapshot at density $n = 1$ and shear rate $\dot{\gamma} = 0.01$ are provided by Figure 4. The transient shear stress for this sample exhibits an overshoot at $t\dot{\gamma} \approx 5$ before reaching a stationary value at $t\dot{\gamma} \gg 50$.

6.2. Uniaxial compression. The model metal has been uniaxially compressed at constant elongation rate $\dot{\epsilon} = 0.01$. Two snapshots are given in Figure 5. During compression the number of layers decreases. We observe spontaneous symmetry breaking; see the inset (top view) of Figure 5. The often quoted "theoretical value" for the critical penetration hardness σ_{c} should be $\sigma_{\mathrm{c}} = c\,G$ with the shear modulus G and $c = c_{\mathrm{th}} = 1/10$. The experimentally observed factor is smaller, $c_{\mathrm{exp}} = 10^{-3} - 10^{-2}$. Our preliminary result is $c_{\mathrm{sim}} \approx 1/50$ being estimated from the simulated normal stress σ_{yy}.

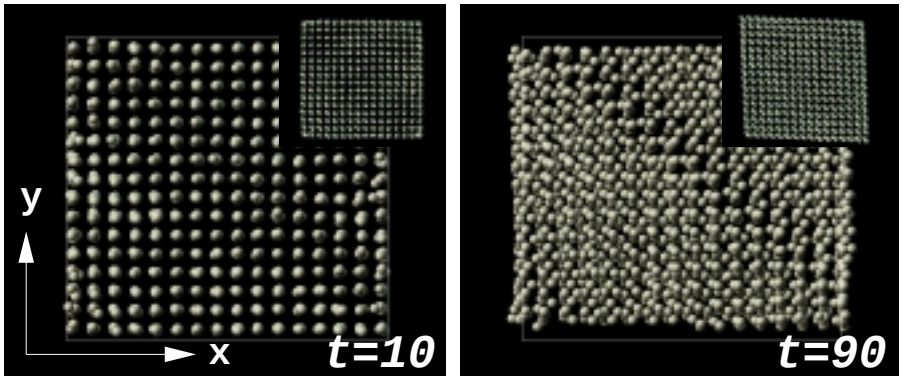

FIG. 5. *NEMD snapshots of EMB ($N = 16800$, $n = \rho_{\rm des} = F_0 = 1$) at times $t = 10$ and $t = 90$ after incession of uniaxial elongational flow (with rate $\dot{\epsilon} = 0.01$ in the y-direction) of an ideal fcc lattice.*

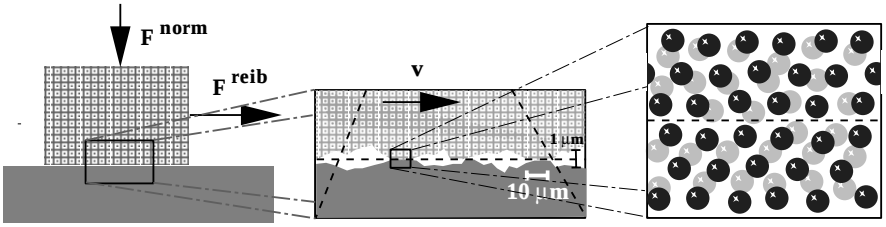

FIG. 6. *Schematic drawing of two metals in contact (load $\mathbf{N} \equiv \mathbf{F}^{\rm norm}$, friction force $\mathbf{F} \equiv \mathbf{F}^{\rm reib}$) where the relative velocity $\mathbf{v}$ is given. Shear stress is buildup within a small amount of contact zones (asperites).*

7. Solid friction. The understanding of friction between two solid surfaces can be traced back to the experiments and descriptions offered by Leonardo da Vinci and Charles Coulomb [36]. Accordingly, sliding two bodies in the presence of solid-solid contacts (cf. Figure 6) requires a friction force $\mathbf{F}$ whose magnitude is proportional to the load $\mathbf{N} \perp \mathbf{F}$ normal to the interface; i.e., $F = \mu N$ with a dimensionless friction coefficient μ. Since the magnitudes of the friction force is independent of the apparent contact area A between the bodies, the established picture is that the shear stress is buildup within a small amount of contact zones (asperites). Their effectively interacting area $\triangle A$ is increasing during a load-induced plastic flow. Typically, the contact zones occupy a small part of the total area, e.g., $\triangle A = 10^{-4} A$, and the area per contact zone is of the order of $(10\mu\mathrm{m})^2$.

For the case of sliding friction we simulate a contact zone at relative motion in the x-direction, with a load and shear gradient in the y-direction; i.e., the load is related to a normal pressure p_{yy}, also called penetration hardness $\sigma_{\rm c} \equiv p_{yy} = N/A$, at the onset of plastic flow. The shear stress $\tau_{xy} = F/\triangle A$ or, alternatively, the shear component of the friction pressure tensor $p_{xy} = -\tau_{xy}$, is "measured."According to the "friction rule" $F = \mu N$ introduced above, one therefore has $\tau = \mu\sigma_{\rm c}$ or $p_{xy} = -\mu\, p_{yy}$ inside contact zones.In order to simulate an interface, we extended the model for

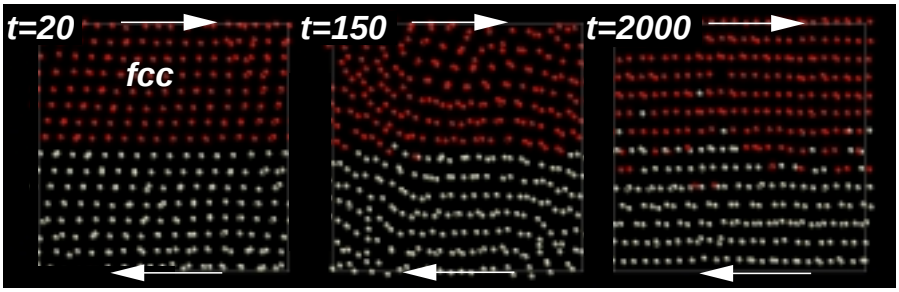

FIG. 7. *NEMD snapshots of EMB ($N = 16800$, $n = \rho_{\mathrm{des}} = F_0 = 1$) at times $t = 20$, $t = 150$, and $t = 2000$ after incession of shear flow with shear rate $\dot{\gamma} = 0.01$ of two commensurate ideal fcc lattices in contact, modeling the process of solid friction. The interfacial parameter $w_{ab} = 1.5$. The figure shows only a part (two-dimensional cut with thickness 3 in reduced units) of the whole system.*

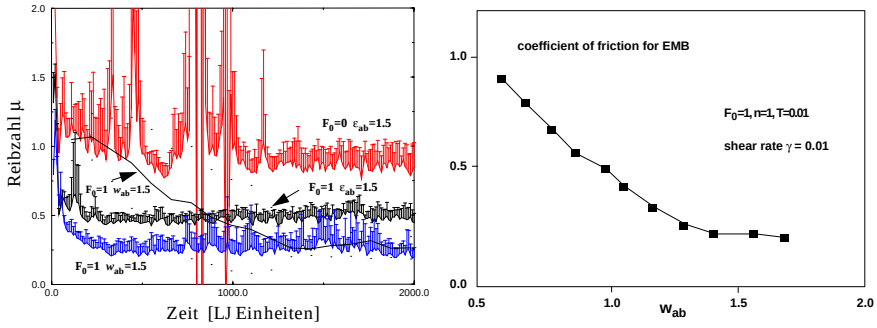

FIG. 8. *Left: The transient friction coefficient μ of the model metal EMB at $n = 1$ vs. time for four different settings:* (a) $F_0 = 0$, $e_{ab} = 1.5$, (b) $F_0 = 1$, $e_{ab} = 1.5$, (c,d) $F_0 = 1$, $w_{ab} = 1.5$. *The simulation runs* (a)–(c) *were started from an ideal fcc lattice; run* (d) *was started from an equilibrium (prerelaxed) sample. The results have been averaged over* 10 *independent initial configurations—with respect to the initial distribution of velocities for cases* (a)–(c). *The results reveal the influence of the interface and the initial condition on the friction behavior. Right: Influence of the interfacial parameter w_{ab} on the friction coefficient of EMB.*

specification of the strength of interaction between particles i, j belonging to the same and to different materials; i.e., we introduce two factors e_{ij} and w_{ij} in front of $\Phi(\mathbf{r}^{ij})$ and $w(\mathbf{r}^{ij})$ in the EMB model equations (2.1)–(2.2). The default values inside the bulk are $\mathrm{e}_{ij} = \mathrm{w}_{ij} = 1$. For two perfect fcc metals blocks with 2056 particles (and periodic boundary conditions in the plane) undergoing solid friction at constant overall shear rate, see Figure 7. Notice that at times $t = 20$ and $t = 2000$, 16 and 14 layers of particles are observed, respectively, due to the reorganization of initially 100 oriented crystal to its final (preferred 111) orientation. The simulated transient behavior of the friction coefficients for four model metals is plotted in Figure 8 (left); it covers experimentally observed behavior [37, 38, 39]. For the presented data the total simulation time was of the order of $10^{-10} - 10^{-9}$s and hence smaller than the minimum "lifetime" of a contact zone 10^{-7}s, to be determined by the typical size of a zone (10μm) divided by a high velocity, e.g., 100 m/s. The dependence of the friction coefficient on w_{ab} is analyzed in the right-hand side of Figure 8.

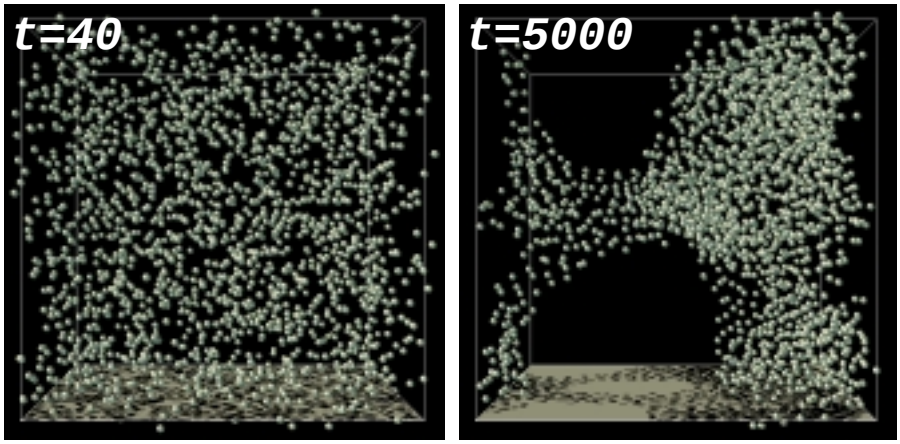

FIG. 9. *Equilibration of an EMB metal sponge at* $T = 0.01$ *(*$N = 2048$*,* $n = 0.3$*,* $\rho_0 = 1$*) obtained via molecular dynamics. Initial configuration: fcc lattice (not shown). Snapshots taken at* $t = 40$ *(left) and* $t = 5000$ *(middle). A hole formed inside the sponge is visible in the projection.*

8. Porous metal structure. A variation of the model potentials introduced above serves to study metal sponges, as will be demonstrated in this section. See [21] for an introduction to this field. The modification concerns the controlled mismatch between preferred local and the global embedding number densities. In order to model a porous metal we choose (bulk, cell wall) density $\rho_{\rm des} = 1$ (reduced units) larger than the overall number density $n \equiv N/V = 0.3$; the cut-off radius h of Φ is set to $h = 1.6$, and the temperature is fixed to $T = 0.01$. This setting allows for the study of the microscopic foundation of (i) the cell shape and diameter, cell wall thickness, further structural parameters, and the formation dynamics of cellular metals, and (ii) the mechanical (elastoplastic) behaviors of metal foams, in order to correlate them with the foam (sponge) structure, e.g., porosity, inhomogeneity, cell size for given foam and bulk densities of a chosen model metal. If $\rho_{\rm des} > n$ for given particle density n, the model metal tends to microphase-separate such that the local embedding density approaches the desired value. As a result, holes surrounded by metal are formed which keep connected, caused by the properties of the glue, and the surface tension seems to be high compared to a simple LJ fluid at same parameters; cf. Figure 9 for the formation (equilibration) step of a EMB model sponge. A result for a larger system consisting of 1.048.576 particles is shown in Figure 10. A comparison with systems which are smaller by a factor 10–20 confirms that the sponge structure is quantitatively independent of system size above $N \approx 10000$ particles under the current conditions. Three pictures out of an animation for a nonequilibrium sponge (subjected to shear) are shown in Figure 11. The series illustrates the effect of the implemented embedded particle potentials on the gluey attributes of EMB compared with a simple LJ fluid. Another illustrative example is shown in Figure 12 for a freestanding EMB sponge subjected to finite strain. One of the open questions concerns the self-similarity of structures upon changing system size, the mechanical properties of the sponge as the function of density. In applications, foams are usually produced with 0.05–0.20 porosity. For our model metal, the porosity is roughly equal to the ratio between particle density and desired embedding density $n/\rho_{\rm des}$. Our preliminary studies on large systems such as in Figure 10 reveal that for given bulk density $\rho_{\rm des}$, total volume V, and foam density n, the ratio between cell wall thickness s and cell diameter

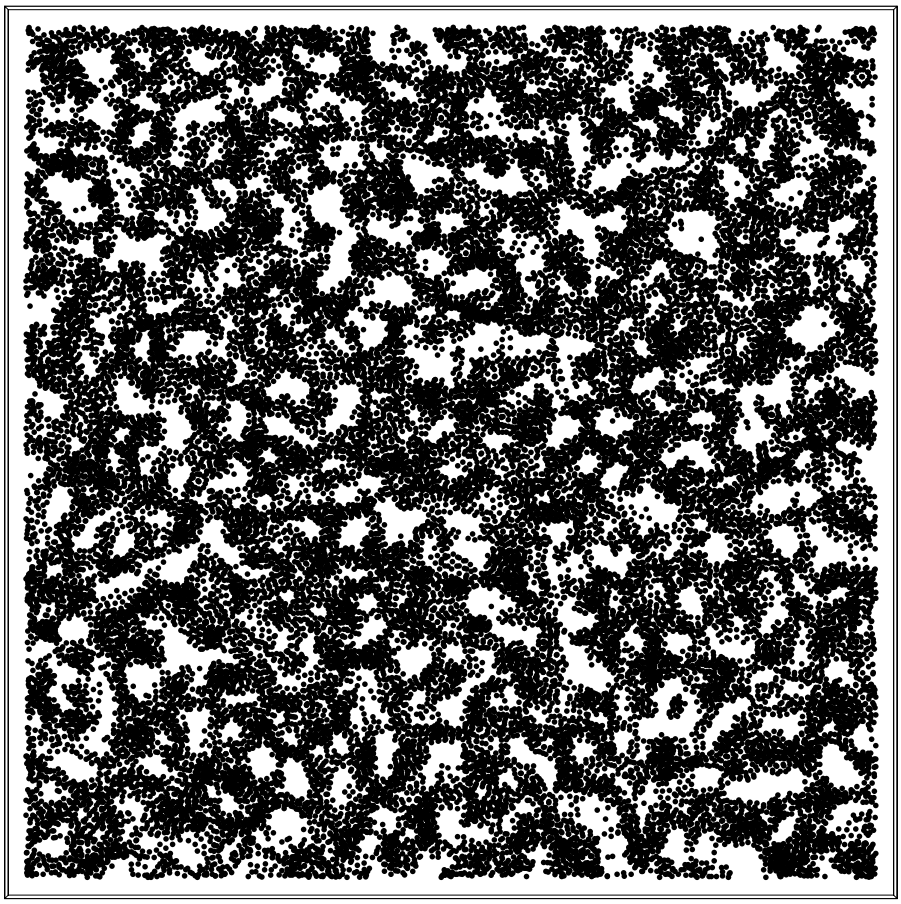

FIG. 10. *Metal sponge at rest (left) consisting of* 1.048.576 *particles after an equilibration period of* 50 *reduced time units (initial configuration: perfect fcc lattice). Parameters: temperature* $T = 0.01$*, preferred local embedding number density* $\rho_0 = 1$*, and overall particle number density* $n = 0.3$*. Plotted are all particles located within a common layer of width* 3% *of the full simulation cell.*

$d \gg s$ behave as $s/d \approx n/(3\rho_{\mathrm{des}})$. For the number density p of pores we simply have $p \propto d^{-3} \propto (n/s\rho_{\mathrm{des}})^3$. It remains to be shown how these relations alter in the course of the dynamics of the formation step.

9. Conclusion. The embedded atom method has been adapted to study solid friction and the mechanical behavior of the model metal EMB. The elastic properties of real metals are reproduced by a set of basic model potentials. NEMD computer simulations are performed to study the dynamics and structural changes of the model metal undergoing elastoplastic shear, a process of solid friction, and an uniaxial compression, in order to analyze plastic yield and transient friction coefficients, where the stress during sliding is built up within asperites on the nm scale. Longer simulation runs are needed to determine values for the penetration hardness with high precision and to analyze the relationship between stress and deformation. It was also demonstrated that a variant of the model metal serves to study large scale metal foams and porous metal structures.

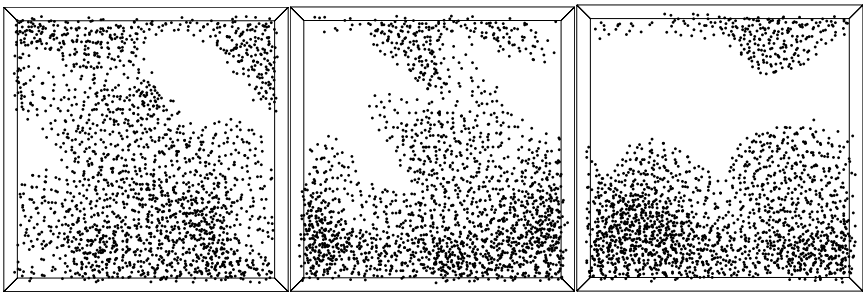

FIG. 11. *EMB metal sponge with $N = 2048$ particles, at temperature $T = 0.01$, particle number density $n = 0.3$, and embedding density $\rho_0 = 1 > n$, subjected to shear deformation with rate $\dot{\gamma} = 0.01$. Snapshot taken at time $t = 20, 100, 500$ (from left to right).*

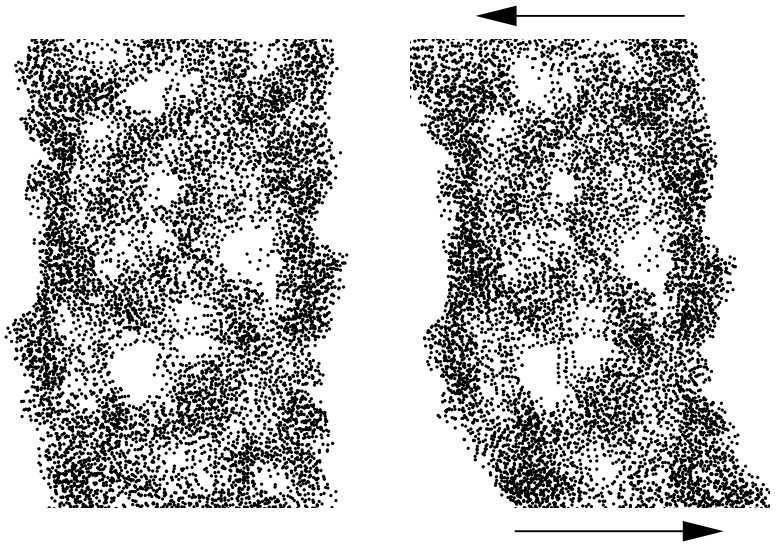

FIG. 12. *Zoom into the system shown in Figure* 10 *in a nonequilibrium situation. Metal sponge at rest (left, subsystem consisting of* 55296 *particles) and subjected to finite shear ($t\dot{\gamma} = 2$) deformation (right) obtained via molecular dynamics (same particles).*

REFERENCES

[1] C. F. MELIUS, C. L. BISSON, AND W. D. WILSON, *Quantum-chemical and lattice-defect hybrid approach to the calculation of defects in metals,* Phys. Rev. B, 18 (1978), pp. 1647–1657.

[2] R. A. JOHNSON, *Relationship between two-body interatomic potentials in a lattice model and elastic constants,* Phys. Rev. B, 6 (1972), pp. 2094–2100.

[3] J. N. GOODIER, in Fracture: An Advanced Treatise, Vol. 2, H. Liebowitz, ed., Academic Press, New York, 1968.

[4] K. FUCHS, *A quantum mechanical calculation of the elastic constants of monovalent metals,* Proc. Roy. Soc. London Ser. A, 153 (1936), pp. 622–639.

[5] K. FUCHS, Proc. Roy. Soc. London Ser. A, 157 (1936), p. 444.

[6] M. J. STOTT AND E. ZAREMBA, *Quasiatoms: An approach to atoms in nonuniform electronic systems,* Phys. Rev. B, 22 (1980), pp. 1564–1583.

[7] J. K. NØRSKOV, *Covalent effects in the effective-medium theory of chemical binding: Hydrogen*

heats of solution in the 3*d metals,* Phys. Rev. B, 26 (1982), pp. 2875–2885.
[8] M. S. Daw and M. I. Baskes, *Semiempirical, quantum mechanical calculation of hydrogen embrittlement in metals,* Phys. Rev. Lett., 50 (1983), pp. 1285–1288.
[9] M. S. Daw and M. I. Baskes, *Embedded-atom method: Derivation and application to impurities, surfaces, and other defects in metals,* Phys. Rev. B, 29 (1984), pp. 6443–6453.
[10] K. W. Jacobsen, *The effective medium theory*, in Many-Atom Interactions in Solids, R. M. Nieminen, Proceedings in Physics 48, M. J. Puska, and M. J. Manninen, eds., Springer, Berlin, 1990, pp. 34–47.
[11] R. A. Johnson, *Implications of the embedded-atom method format*, in Many-Atom Interactions in Solids, Proceedings in Physics 48, R. M. Nieminen, M. J. Puska, and M. J. Manninen, eds., Springer, Berlin, 1990, pp. 85–102.
[12] M. C. Desjonqures, D. Spanjaard, C. Barreteau, and F. Raouafi, *Stability of metal vicinal surfaces revisited,* Phys. Rev. Lett., 88 (2002), article 056104.
[13] K. Miwa and A. Fukumoto, *First-principles study on* 3*d transition-metal dihydrides,* Phys. Rev. B, 65 (2002), article 155114.
[14] P. Biswas, *Vibrational properties of amorphous silicon from tight-binding O(N) calculations,* Phys. Rev. B, 65 (2002), article 125208.
[15] F. J. Cherne, M. I. Baskes, and P. A. Deymier, *Properties of liquid nickel: A critical comparison of EAM and MEAM calculations,* Phys. Rev. B, 65 (2002), article 024209.
[16] P. Ballo and V. Slugen, *Atomic simulation of grain-boundary sliding and migration in copper,* Phys. Rev. B, 65 (2002), article 012107.
[17] F. Celestini and J.-M. Debierre, *Measuring kinetic coeeficients by molecular dynamics simulation of zone melting,* Phys. Rev. E, 65 (2002), article 041605.
[18] A. van de Walle and G. Ceder, *The effect of lattice vibrations on substitutional alloy thermodynamics,* Rev. Mod. Phys., 74 (2002), pp. 11–45.
[19] P. Hohenberg and W. Kohn, *Inhomogeneous electron gas,* Phys. Rev. B, 136 (1964), pp. 864–871.
[20] M. J. Puska, R. M. Nieminen, and M. Manninen, *Atoms embedded in an electron gas: Immersion energies,* Phys. Rev. B, 24 (1981), pp. 3037–3047.
[21] J. Banhart, M. F. Ashby, and N. A. Fleck, eds., *Metal foams and porous metal structures*, in Proceedings of the 1st International Conference on Metal Foams and Porous Metal Structures, Bremen, Germany, 1999, pp. 14–16.
[22] L. J. Gibson, M. F. Ashby, J. Zhang, and T. C. Triantafillou, *Failure surfaces for cellular materials under multiaxial loads.* I: *Modeling,* Int. J. Mech. Sci., 31 (1989), pp. 635–663.
[23] A. F. Bastawros, H. Bart-Smith, and A. G. Evans, *Experimental analysis of deformation mechanisms in a closed-cell aluminum alloy foam,* J. Mech. Phys. Solids, 48 (2000), pp. 301–322.
[24] B. L. Holian, A. F. Voter, N. J. Wagner, R. J. Ravelo, S. P. Chen, W. G. Hoover, C. G. Hoover, J. E. Hammerberg, and T. D. Dontje, *Effects of pairwise versus many-body forces on high-stress plastic deformation,* Phys. Rev. A, 43 (1991), pp. 2655–2661.
[25] H. Rafii-Tabar, *Modelling the nano-scale phenomena in condensed matter physics,* Phys. Rep., 325 (2000), pp. 239–310.
[26] F. Herman and S. Skillman, *Atomic Structure Calculations,* Prentice-Hall, Englewood Cliffs, NJ, 1963.
[27] S. Hess and M. Kröger, *Elastic and plastic behavior of model solids*, Tech. Mech., 22 (2002), pp. 79–88.
[28] W. G. Hoover and S. Hess, *Anisotropic plasticity with embedded-atom potential,* Phys. A, 267 (1999), pp. 98–110.
[29] M. P. Allen and D. J. Tildesley, *Computer Simulation of Liquids,* Clarendon Press, Oxford, UK, 1987.
[30] M. Kröger, W. Loose, and S. Hess, *Structural changes and rheology of polymer melts via nonequilibrium molecular dynamics,* J. Rheol., 37 (1993), pp. 1057–1080.
[31] M. Kröger, C. Luap, and R. Muller, *Polymer melts under uniaxial elongational flow: Stress-optical behavior from experiments and NEMD computer simulations,* Macromolecules, 30 (1997), pp. 526–539.
[32] M. Kröger and S. Hess, *Solid friction studied via non-equilibrium molecular dynamics computer simulations,* ZAMM, 90 (2000), Suppl. 1, pp. 48–52.
[33] A. Green and P. Naghdi, *A general theory of an elastic-plastic continuum,* Arch. Ration. Mech. Anal., 18 (1965), pp. 251–281.
[34] A. Green and P. Naghdi, *Some remarks on elastic-plastic deformation at finite strain,* Internat. J. Engrg. Sci., 9 (1971), pp. 1219–1229.
[35] W. Loose and S. Hess, *Rheology of dense model fluids via nonequilibrium molecular dynamics:*

Shear thinning and ordering transition, Rheol. Acta, 28 (1989), pp. 91–99.

[36] F. P. Bowden and D. Tabor, *The Friction and Lubrication of Solids*, 2nd ed., Clarendon Press, Oxford, UK, 1954.

[37] Z. Xia, W. A. Curtin, and P. W. M. Peters, *Multiscale modeling of failure in metal matrix composites*, Acta Mat., 49 (2001), pp. 273–287.

[38] A. Matuszak, *Factors influencing friction in steel sheet forming*, J. Mat. Proc. Tech., 106 (2000), pp. 250–253.

[39] E. Pollak, G. Gershinsky, Y. Georgievskii, and G. Betz, *Microscopic and macroscopic estimates of friction: Application to surface diffusion of copper,* Surf. Sci., 365 (1996), pp. 159–167.

[40] I. Stankovic, M. Kröger, and S. Hess, *Recognition and analysis of local structure in polycrystalline configurations*, Comput. Phys. Comm., 145 (2002), pp. 371–384.